Energy Storage Materials 15 (2018) 124–130

Contents lists available at ScienceDirect

Energy Storage Materials

journal homepage: www.elsevier.com/locate/ensm

Defect-rich carbon fiber electrocatalysts with porous graphene skin for flexible solid-state zinc–air batteries

Hao-Fan Wang, Cheng Tang, Bin Wang, Bo-Quan Li, Xiaoyang Cui, Qiang Zhang*

Beijing Key Laboratory of Green Chemical Reaction Engineering and Technology, Department of Chemical Engineering, Tsinghua University, Beijing 100084, China

ARTICLE INFO

Keywords:
Graphene nanosheets
Metal-free electrocatalyst
Flexible solid-state zinc–air battery
Oxygen reduction reaction
Oxygen evolution reaction
Energy electrocatalysis

ABSTRACT

Rechargeable flexible Zn–air batteries have attracted great attentions as promising next-generation energy storage devices for portable and wearable electronics. Bifunctional oxygen evolution reaction (OER) and oxygen reduction reaction (ORR) electrocatalysts on the air electrode are critical for improving the energy storage performance of Zn–air batteries. Free-standing electrocatalysts with superb OER/ORR reactivity render promising flexible power sources for the wearable and stretchable devices. In this contribution, a metal-free electrocatalyst based on surface modification of flexible carbon cloth is proposed. A coaxial cable-like structure with carbon fiber skeleton coated by nanostructured porous and defect-rich graphene skin is *in situ* fabricated through a facile H_2 etching approach. With abundant heteroatoms and defects as active sites, the nanocarbon shells coated carbon cloth exhibits excellent OER/ORR bifunctional activity. The OER and ORR current densities on graphene skin modified carbon fiber are 20 and 3 times higher than those of pristine carbon cloth, respectively. This emerging carbon cloth derived electrocatalyst with porous graphene skin also serves as the air electrode in a rechargeable flexible solid-state Zn air battery with polymer gel electrolyte, and demonstrates stable charge/discharge cycling even under bending. This strategy of constructing nanostructures directly on carbon fibers benefits the rational design of flexible and functionalized materials for electrocatalytic energy applications.

1. Introduction

Zn–air batteries have been investigated as promising new energy devices for their high energy densities and relatively low costs [1–5]. It is increasingly attractive to explore solid-state Zn–air batteries that possess the advantages of high flexibility and intrinsic safety [6–17]. The solid-state Zn–air batteries can fulfill the requirements for wearable and stretchable electronics [18]. One critical challenge for Zn–air batteries is the low energy conversion efficiency on the air electrode. The conversion between oxygen and water takes place on the air electrode during the charge/discharge process, including the oxygen evolution reaction (OER, charging process) and the oxygen reduction reaction (ORR, discharging process) [19]. Both the two reactions are four-electron processes with complicated reaction pathways and high overpotentials [20–22]. Therefore, OER/ORR bifunctional electrocatalysts are strongly considered to render the Zn–air batteries with enhanced energy storage performance.

Various non-precious metal electrocatalysts, including transition metal compounds [23–25] and carbon nanomaterials [26–29], exhibit superb bifunctional activity when applied in Zn–air batteries [30–32]. However, most of the electrocatalysts are in powder state macroscopically, and require further electrode fabrication by attaching to carbon cloths or carbon fiber papers to fabricate Zn–air batteries. The uniformity and stability of the air electrode is highly depended on the materials processing in each laboratory. Therefore, full demonstration of electrocatalyst in a flexible metal–air battery remains a grand challenge. If a three-dimensional flexible OER/ORR bifunctional electrocatalyst can be achieved, the Zn–air batteries are expected to be more easily and efficiently obtained in a flexible state with solid state electrolyte.

Carbon cloth is commonly used as the catalyst substrate for the air electrodes of Zn–air batteries, because of its advantages of high stability, excellent conductivity, and flexibility [33–36]. Since carbon cloths hardly have any catalytic activity, bifunctional OER/ORR catalysts are deposited on carbon cloths to lower the overpotential of Zn–air batteries. Carbon cloths are composed of dense arrays of carbon fibers (Fig. S1). Considering that carbon-based materials have been widely investigated as OER/ORR bifunctional electrocatalysts, it is

* Corresponding author.
E-mail address: zhang-qiang@mails.tsinghua.edu.cn (Q. Zhang).

https://doi.org/10.1016/j.ensm.2018.03.022
Received 30 January 2018; Received in revised form 7 March 2018; Accepted 25 March 2018
Available online 27 March 2018

promising to activate carbon fibers by rational surface modification. Consequently, the activated carbon cloth can serve directly as a free-standing and flexible air electrode in a Zn–air battery without any other additional electrocatalyst component.

The carbon atoms in polyacrylonitrile (PAN) based carbon fibers are arranged in a similar manner to graphite. In details, the carbon atoms are in a regular hexagonal pattern and the graphitic sheets are connected by van der Waals interactions, preferentially aligned along the PAN based carbon fiber axis [37]. Therefore, the electrocatalytic performance can be enhanced by the exfoliation of carbon fibers at the surface to generate few-layer graphene structures, and the design principles of graphene-based electrocatalysts [38–40], such as introducing heteroatoms and defects, enlarging the surface area, are expected to further improve the performance of the fiber based electrocatalysts.

In this contribution, we proposed a high-temperature H_2 etching method on carbon fibers to obtain an emerging core-shell structure of carbon fibers coated by active porous graphene nanosheet skin. The internal carbon fiber core constitutes a free-standing flexible and conductive skeleton at the macroscale, while the outer nanostructured porous carbon shell affords enriched defects and high surface area at the nanoscale. This defect-rich, surface porous, coaxial cable-like structure is expected to exhibit high electrocatalytic activity.

2. Results and discussion

The synthesis process of the carbon fiber@porous carbon structure is shown in Fig. 1. After washed by acetone, 2.0 M sulfuric acid, and deionized water successively, the pristine carbon cloth (CC, Fig. 1a), with stacked graphite sheets on the surface, was oxidized by the immersion in a mixed solution of H_2O_2 and concentrated H_2SO_4 for 12 h. On the surface of the as-oxidized carbon cloth (o-CC, Fig. 1b), graphene-like nanosheets are exfoliated, and oxygen-containing groups are generated. The o-CC was then placed in a horizontal quartz tube reactor, and heated to 950 °C under Ar protection. Then H_2 (40 mL min^{-1}) was introduced into the reactor for 5 min. During this process, carbon atoms were etched by hydrogen to generate hydrocarbons. Consequently, porous and defective structures were fabricated on the surface of carbon fibers. After cooled to room temperature under Ar protection, the surface porous carbon cloth (denoted as o-CC-H_2, Fig. 1c) was obtained. All carbon cloth samples were kept in deionized water to enhance hydrophilicity [36].

Fig. 2a exhibits the scanning electron microscopy (SEM) image of a carbon fiber in o-CC-H_2. Macropores with an average diameter of ~ 100 nm are uniformly distributed on the outer surface of carbon fibers, and statistically occupy ~ 40% of the surface area. Compared with plasma-etched carbon fibers or vertical aligned graphene nanosheets on carbon fibers, smaller, more ordered, and more abundant pores are generated [41–43]. An energy-dispersive X-ray spectroscopy (EDS) mapping test was also performed on o-CC-H_2, and C and O elements were observed to distribute uniformly on the surface of the catalyst (Fig. S2). In the transmission electron microscopy (TEM) images of o-CC-H_2 (Figs. 2b and 2c), two kinds of structures can be observed on the carbon fiber surface. On one hand, the exfoliated graphene sheets are uniformly distributed on the surface of o-CC-H_2 (Fig. 2b), with a thickness of about 20 nm. The exfoliation also occurs on o-CC (Fig. S3), but not on CC sample (Fig. S4), indicating that the oxidation process is critical for the formation of the external graphene nanosheet skin. On the other hand, the surface pores (Fig. 2c) are expected to afford more active sites and larger surface area, which is benefited from the H_2-etching on the surface of carbon fibers and constructed by curving graphene materials.

To probe the formation mechanism, the high temperature treated o-CC only with Ar flow (o-CC-Ar) and high temperature H_2 etched CC (CC-H_2) were also synthesized. On the surface of CC (Fig. S5), o-CC (Fig. S6), and o-CC-Ar (Fig. S7), no pore can be observed, confirming that the gasification reaction of carbon at high temperature requires the assistance of hydrogen and induces pore formation on the surface of carbon fibers. Compared with o-CC-H_2, CC-H_2 contains fewer and smaller pores (Fig. S8). It can be attributed to the exfoliated graphene layer rendered by the pre-oxidation process on o-CC that affords larger surface area and more oxygen-containing groups for H_2 adsorption, thus facilitating the H_2-etching process.

These porous graphene skin is with a thickness of ca. 300 nm on o-CC-H_2, as shown by the cross-section SEM image in Fig. 2d. The internal part of the carbon fiber remains solid, ensuring the robust strength and excellent electrical conductivity of free-standing carbon fiber based electrocatalysts. This coaxial cable-like configuration is favorable for full exposure of active sites and efficient electron transfer, and is expected to boost excellent electrocatalytic activity in energy electrocatalysis [44].

X-ray photoelectron spectroscopy (XPS) analyses were performed to characterize the chemical composition of free-standing carbon fiber based electrocatalysts. The oxygen atomic content of o-CC-H_2 is 12.6%, significantly higher than that of CC (5.6%). The high oxygen content of o-CC-H_2 can be attributed to the oxidation process and the chemical

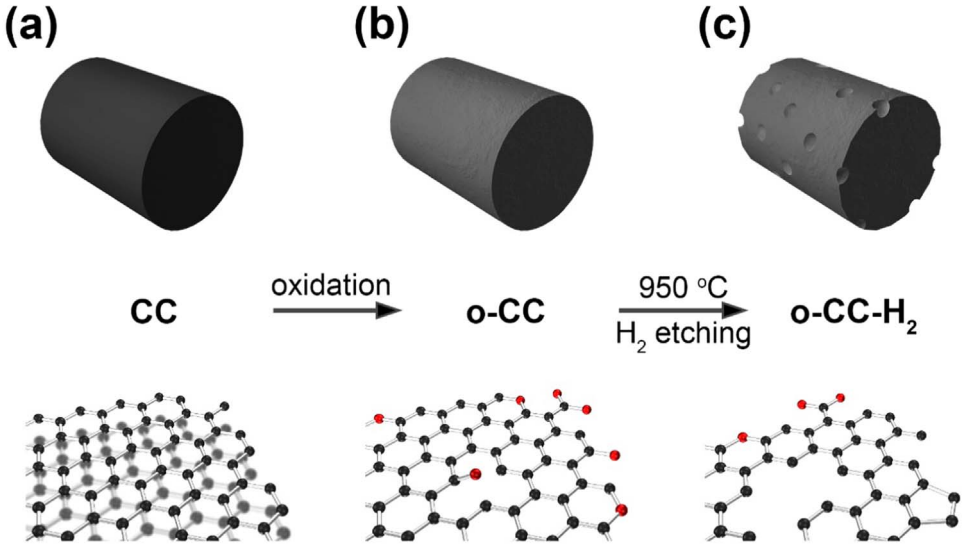

Fig. 1. Schematic illustration of the synthesis of o-CC-H_2 and the morphology evolution from (a) CC to (b) o-CC and then (c) o-CC-H_2. The black balls represent for carbon atoms, and the red balls represent for oxygen atoms.

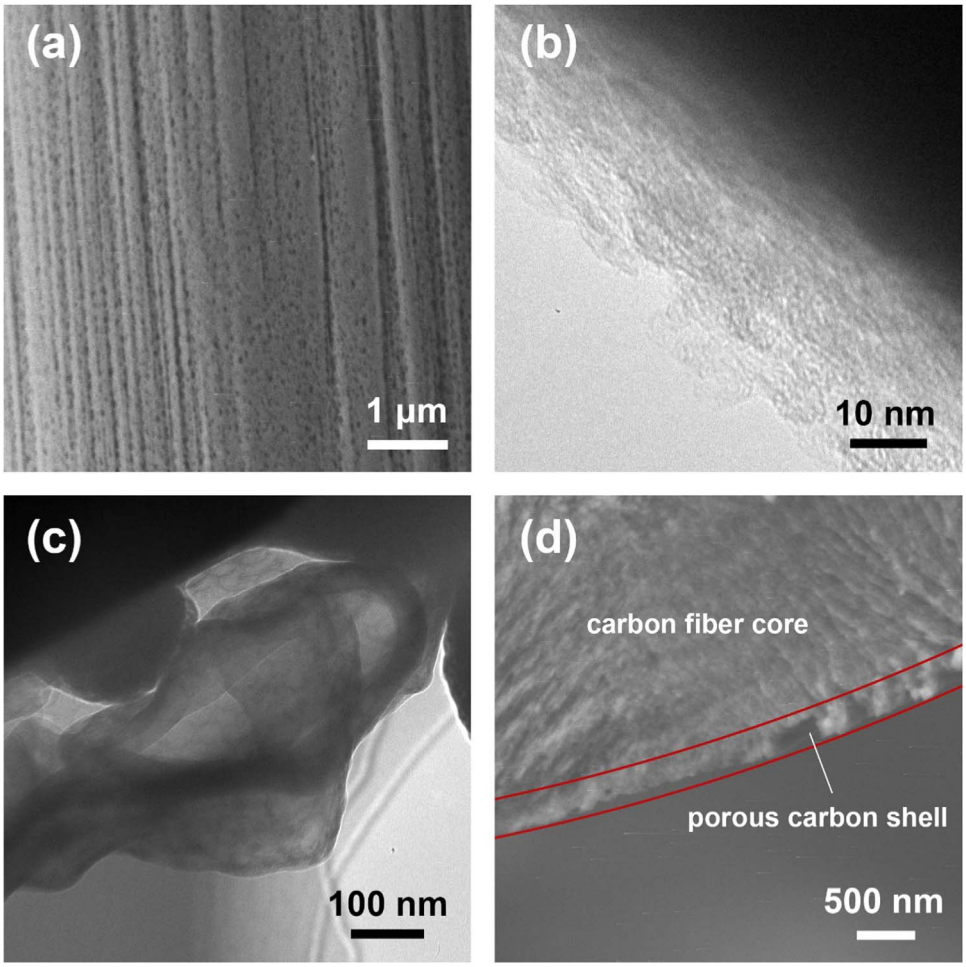

Fig. 2. The morphology of o-CC-H_2. (a) SEM image of a carbon fiber in o-CC-H_2. (b-c) TEM images of o-CC-H_2. (d) SEM image of a cross section of o-CC-H_2.

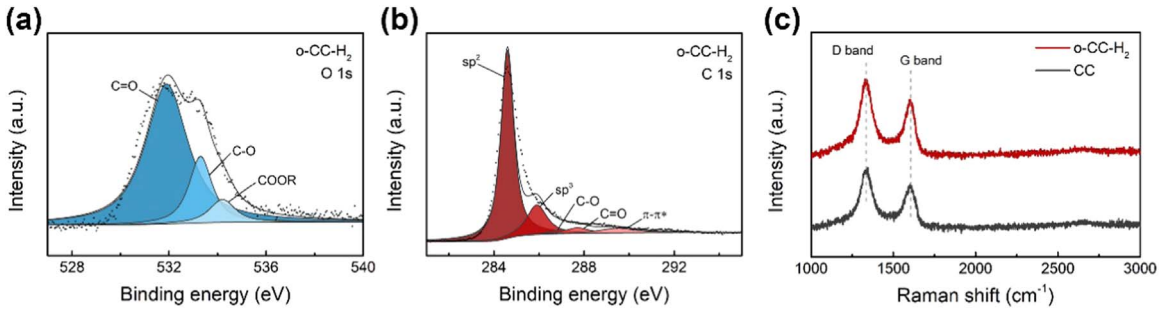

Fig. 3. Structural characterizations of o-CC-H_2 and CC. (a) High resolution O 1s XPS spectrum of o-CC-H_2. (b) High resolution C 1s XPS spectrum of o-CC-H_2. (c) Raman spectra of o-CC-H_2 and CC.

adsorption on the porous surface during the immersion in deionized water. High resolution XPS O 1s spectrum is shown in Fig. 3a. The peaks at 531.9, 533.3, and 534.2 eV are identified as the peaks of three kinds of oxygen-containing functional groups, –C=O, –C–O, and –COOR, respectively [45]. The content of –C=O type functional groups among all oxygen-containing groups on the surface of o-CC-H_2 is calculated to be 74%, While this content is 54% for CC (See the XPS O 1s spectrum of CC in Fig. S9). Oxygen heteroatoms can regulate the electronic structure of adjacent carbon atoms, influencing the adsorption of reactants (OH^- for OER and O_2 for ORR) on carbon atoms, thus affect the electrocatalytic performances. Considering the three oxygen functional groups, –C–O and –COOR convert to negatively charged –$C–O^-$ and $–COO^-$ in alkaline electrolyte of Zn–air batteries, which repulse OH^- and O_2 and scarcely contribute to electrocatalytic reactivity. Meanwhile, the carbon atom in –C=O remains positively charged due to the electron-withdrawing effect of the adjacent oxygen in the alkaline electrolyte despite the alkaline conditions [46]. The positive charged carbon facilitates the adsorption of reactants, thereby increasing bifunctional OER and ORR reactivity. The total oxygen content and the content of oxygen in –C=O groups of CC, o-CC and o-CC-H_2 are compared in Fig. S10. The larger content of –C=O groups in o-CC-H_2 is expected to boost a better performance for OER/ORR electrocatalysis.

The defects (such as vacancies, lattice reconstruction, and nonhexagonal topologies) significantly contribute to OER/ORR reactivity [26,38,47,48]. The XPS C 1s spectrum of o-CC-H_2 is shown in Fig. 3b. The five peaks at 284.6, 285.9, 286.9, 287.7, and 289.5 eV are assigned to sp^2 carbon, sp^3 carbon, –C–O groups, –C=O groups and π–π* shake-up satellites, respectively [41,49]. Compared with CC (Fig. S11), the calculated sp^2/sp^3 ratio of o-CC-H_2 is lower (4.0 vs. 6.2), indicating more defects in o-CC-H_2. Raman spectrum analysis was also

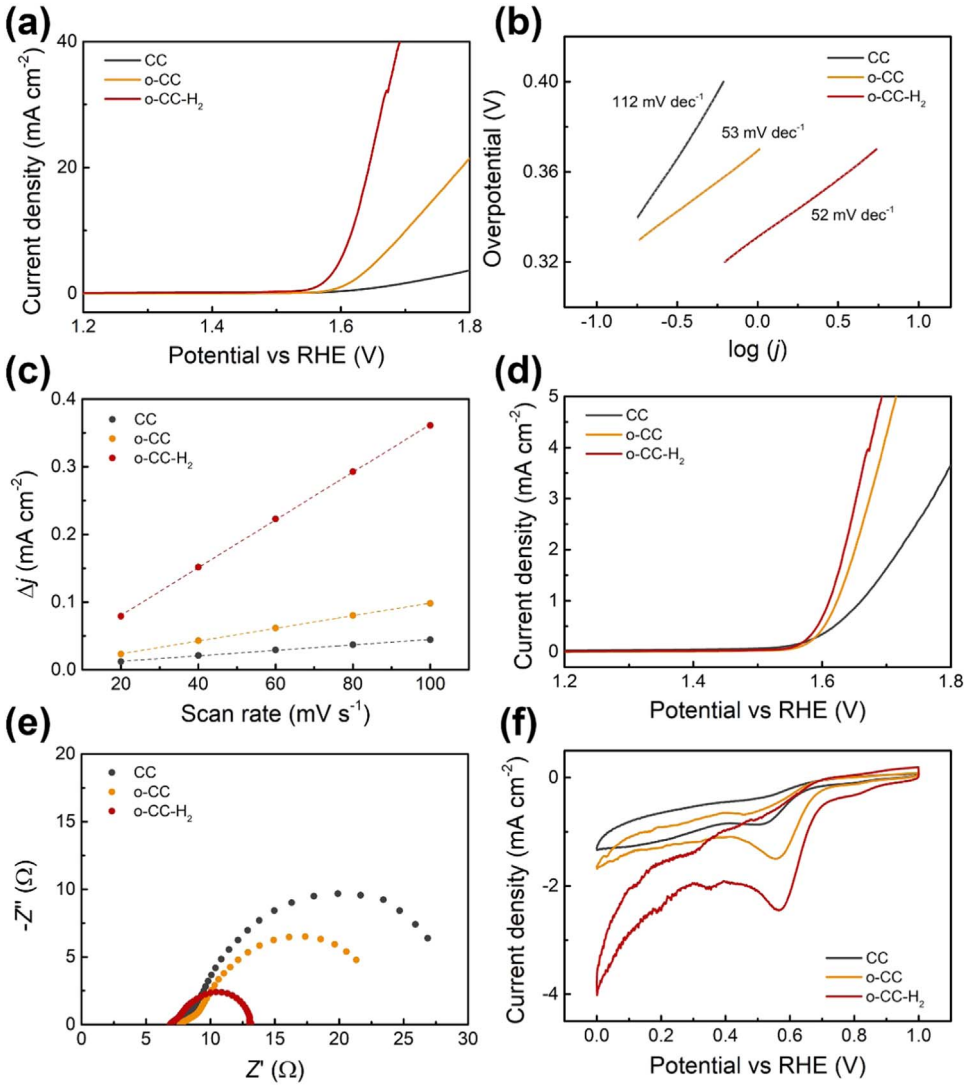

Fig. 4. (a) The OER LSV plots of CC, o-CC, and o-CC-H_2 at a scan rate of 10 mV s^{-1}. (b) The Tafel plots of CC, o-CC and o-CC-H_2. (c) Charging current density differences plotted against scan rates. The linear slope, equivalent to twice the double-layer capacitance C_{dl}, was employed to represent the ECSA. (d) The OER current densities based on ECSA by assuming the ECSA of CC to be 1. (e) Nyquist plots obtained from EIS measurements at a potential of 1.70 V vs. RHE. (f) The CV plots of CC, o-CC and o-CC-H_2 at a scan rate of 50 mV s^{-1}. All electrochemical tests are performed in O_2-saturated 0.10 M KOH electrolyte at 25 °C.

applied to probe the defects of the carbon cloth. Fig. 3c exhibits the Raman spectra of CC and o-CC-H_2. The o-CC-H_2 exhibits a higher I_D/I_G ratio over CC (1.78 vs. 1.69). This higher I_D/I_G ratio verifies the defect-rich structure of o-CC-H_2. The defects can be attributed to the porous graphene skin, including the exfoliated graphene sheets and surface pores shown by the SEM and TEM images. Consequently, it can be inferred that with the defects, heteroatoms, and the nanostructured surface, both OER and ORR reactivity of o-CC-H_2 is expected to be significantly enhanced.

The electrocatalytic performance of o-CC-H_2 was probed in oxygen saturated 0.10 M KOH electrolyte. The surface-nanostructured o-CC-H_2 exhibits superior activity considering both OER and ORR. The OER current density of o-CC-H_2 is much higher than that of o-CC and CC from the OER linear sweep voltammetry (LSV) plots (Fig. 4a). The potential to achieve a 10.0 mA cm^{-2} current density (E_{10}) for o-CC-H_2 is 1.618 V vs. reversible hydrogen electrode (RHE), while the current density of CC and o-CC at the same potential are 0.5 and 2.0 mA cm^{-2}, respectively. Moreover, the OER activity of o-CC-H_2 also surpasses CC-H_2 and o-CC-Ar (Fig. S12), confirming that the porous, defect-rich electrocatalyst possesses superior OER reactivity.

The electrocatalytic activity can be attributed to two aspects, the reactivity and the accessibility [40,50]. The reactivity stands for the intrinsic activity of the active sites. Fig. 4b exhibits the Tafel plots derived from the LSV plots and o-CC-H_2 exhibits the lowest Tafel slope of 52 mV dec^{-1}. This low Tafel slope indicates high intrinsic activity of o-CC-H_2 due to the heteroatoms and defects. The role of doped oxygen atoms has been demonstrated in previous works [45,51,52]. The –C=O functional group is widely considered to be effective active centers in OER electrocatalysis. The defects can also regulate the electronic structure of the carbon atoms by the atypical arrangement of them, thus boosting the catalytic activity [26,47,53,54].

The accessibility signifies the active sites should be accessible to the reactants, the electrolyte, and the electrons. Favorable electrocatalysts are required to have high electrochemical active surface area (ECSA) and low resistance. The ECSA is characterized by measuring the double layer capacity (C_{dl}) using the cycling voltammetry (CV) method. The difference of the charging current density and the discharging current density, Δj, is in a linear function of the CV scan rate (Fig. 4c). The slope is twice the C_{dl}, which is proportional to the ECSA. The ECSA of o-CC-H_2 is about 3.8 times of o-CC, and 8.7 times of CC. This high ECSA can be attributed to the oxygen-rich, porous surface of o-CC-H_2. Fig. 4d shows the specific OER current density based on the ECSA, which directly exhibits the intrinsic activity of active sites. Assuming the ECSA of CC to be 1, the relative ECSA values of o-CC and o-CC-H_2

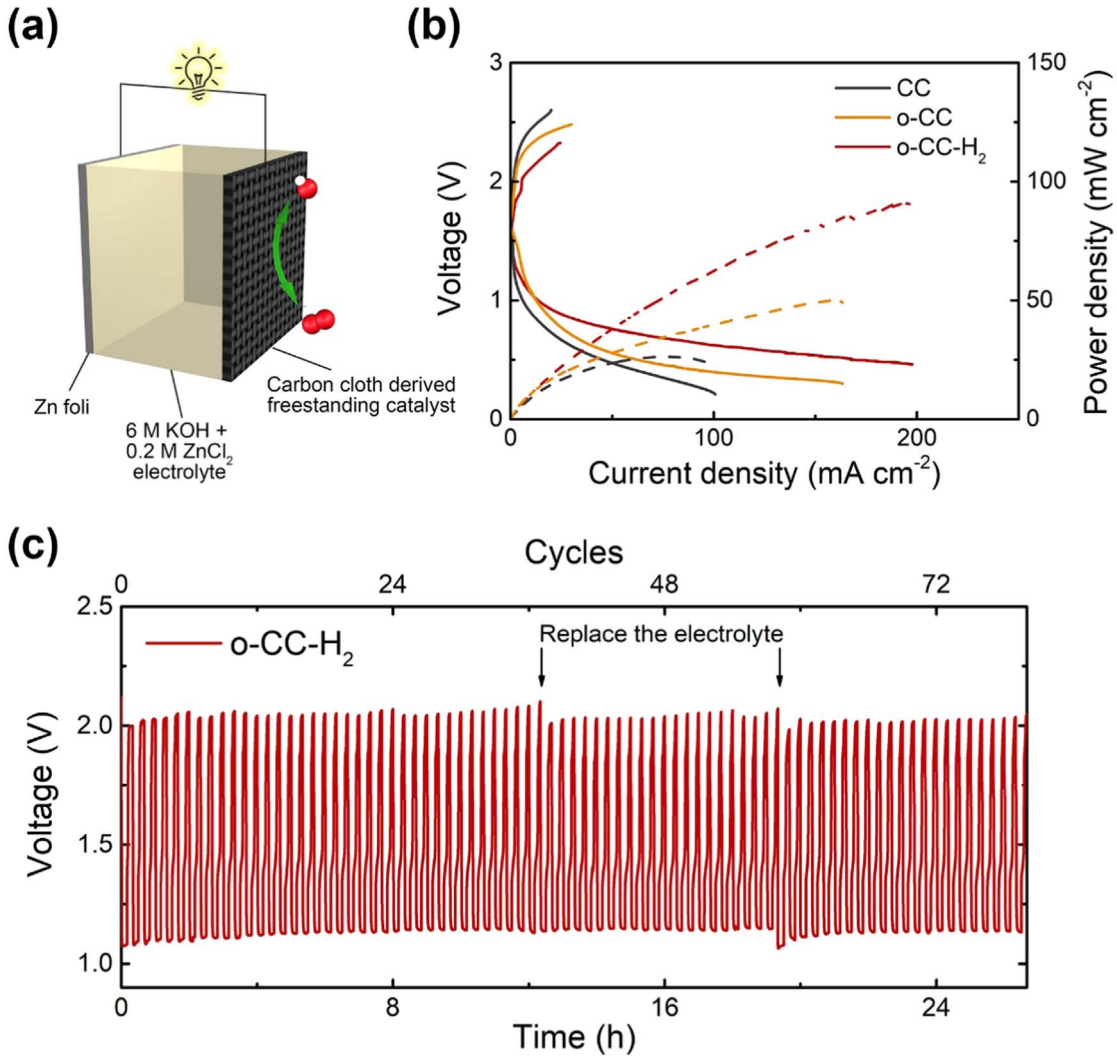

Fig. 5. Conventional Zn–air battery performances with o-CC-H_2 and CC cathode. (a) The schematic diagram of conventional Zn–air battery. (b) Charge/discharge polarization and power density curves of o-CC-H_2 and CC. The scan rate is 10 mV s^{-1}. (c) Long-time galvanostatic cycling performance of Zn–air battery at the current density of 2.0 mA cm^{-2} with o-CC-H_2 as air cathode.

turn out to be 2.3 and 8.7. The o-CC-H_2 is with the highest current density, verifying that the superior OER activity is attributed by the high reactivity and high accessibility together. The electrochemical impedance spectroscopy (EIS) was performed at 1.70 V vs. RHE in a frequency range of 0.1–10^5 Hz with an amplitude of 5.0 mV. In the Nyquist plots (Fig. 4e), o-CC-H_2 shows a much lower resistance in working condition, consistent well with the high catalytic activity.

The ORR performance is characterized by CV tests (Fig. 4f) at the scan rate of 50 mV s^{-1}. All the carbon cloth samples display oxygen reduction peaks in the CV plots. The peak potential of o-CC-H_2, o-CC, and CC are 0.565, 0.554, and 0.466 V, respectively. Moreover, o-CC-H_2 exhibits a higher peak current density of 2.45 mA cm^{-2} than o-CC (1.50 mA cm^{-2}) and CC (0.86 mA cm^{-2}). The positively shifted peak potential and the highest peak current density verify the superior ORR activity of o-CC-H_2, which is also contributed from the porous and defective surface structure. The ORR performances of the catalysts were also tested at a low scan rate of 10 mV s^{-1}, and o-CC-H_2 also exhibits the highest current density (Fig. S13). However, the ORR current densities display severe turbulence at the high-overpotential mass transport-limited region. Therefore, high-scan rate CV tests are utilized to characterize the ORR performances. The OER/ORR performances of o-CC-H_2 and other reported free-standing carbon-based bifunctional electrocatalysts [34,41,55] are listed in Table S1. It's indicated that o-CC-H_2 exhibits good performance as a carbon cloth derived material, and the activity can be further improved by the doping of other heteroatoms.

The OER and ORR stability of o-CC-H_2 was evaluated by long-time CV tests. The catalyst was cycled between 0.00 and 1.80 V vs RHE in O_2-saturated 0.10 M KOH electrolyte at the scan rate of 100 mV s^{-1}. OER LSV plots and ORR CV plots were tested before cycling and after 200, 600 and 900 cycles, respectively (Fig. S14). The E_{10} of OER and the peak potential of ORR were also presented in Fig. S14. The o-CC-H_2 showed good OER and ORR stability after 900 cycles (9 h).

Demonstrated as an efficient bifunctional electrocatalyst for OER and ORR, the nanostructured porous carbon coated carbon cloth, o-CC-H_2, was then employed as the air electrode in a conventional liquid Zn–air battery. The Zn–air battery was fabricated using a homemade plastic cell, in which 6.0 M KOH aqueous solution with 0.20 M $ZnCl_2$ served as the electrolyte (Fig. 5a). Pristine carbon cloth (CC) was used as the control sample. The discharge and charge curves and power density of o-CC-H_2, o-CC and CC are shown in Fig. 5b. The porous graphene skins modified o-CC-H_2 exhibit a higher peak power density of 91.4 mW cm^{-2} than o-CC (50.0 mW cm^{-2}) and pristine CC (26.3 mW cm^{-2}). The specific capacity calculated based on the galvanostatic discharge curve is 707 mAh g^{-1} for o-CC-H_2 at the current density of 20 mA cm^{-2} (Fig. S15). The cycle stability was tested at the charge/discharge current density of 2.0 mA cm^{-2} (Fig. 5c). The Zn–air battery with o-CC-H_2 as air electrode exhibits an initial charge/

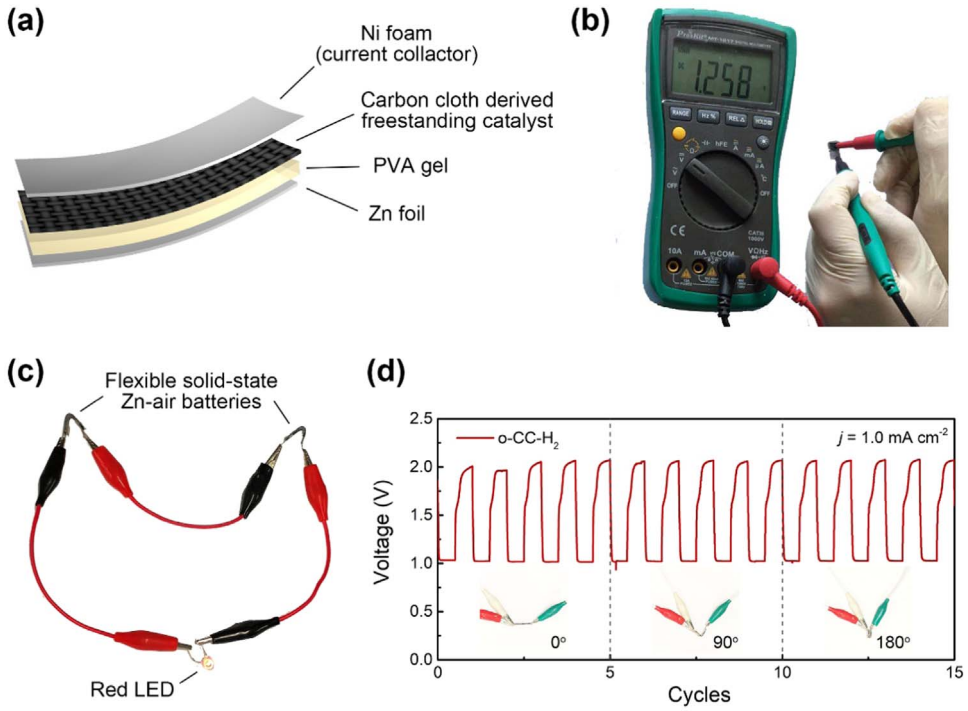

Fig. 6. Flexible solid-state Zn–air battery performances with o-CC-H_2 Cathode. (a) The schematic diagram of flexible solid-state Zn–air battery. (b) Photograph of the solid Zn–air battery, showing an open-circuit voltage of 1.258 V. (c) Photograph of two bended Zn–air batteries connected in series lighting a red LED. (d) Galvanostatic charge/discharge cycling curves at 1.0 mA cm^{-2} and 2 min per cycle under different bending angles.

discharge voltage of 2.00/1.08 V and a voltage gap of 0.92 V. The charge/discharge voltage becomes 2.05 V/1.13 V and a voltage gap remains 0.92 V after 80 cycles (more than 26 h). For comparison, at the same current density of 2.0 mA cm^{-2}, the o-CC and CC cathode exhibit charge/discharge voltage gaps of 1.21 and 1.25 V, respectively (Fig. S16). The superior Zn–air battery performance of o-CC-H_2 over CC is attributed to the higher OER and ORR activity originated from the surface-porous, defect-rich and coaxial cable-like structure of o-CC-H_2.

Flexible and wearable electronic devices have attracted much interest in recent years, and free-standing materials show much potential in these devices. In this contribution, a flexible rechargeable Zn–air battery was fabricated using o-CC-H_2 as the air cathode. The configuration of the flexible Zn–air battery is illustrated in Fig. 6a, with o-CC-H_2 as the air cathode, Zn foil as the anode, alkaline poly(vinyl alcohol) (PVA) gel as the electrolyte, and pressed Ni foam as the current collector. The PVA gel is filled with KOH and $ZnCl_2$, delivering considerable ionic conductivity and mechanical flexibility for flexible Zn–air batteries. The open-circuit voltage is measured to be 1.258 V (Fig. 6b). Two single bended batteries connected in series are able to light a right light-emitting diode (LED), which operates at a minimum voltage of 2.0 V (Fig. 6c). Galvanostatic charge/discharge test was performed at the current density of 1.0 mA cm^{-2}, with 1 min discharge process and 1 min charge process as one cycle (Fig. 6d). The flexible Zn–air battery with o-CC-H_2 cathode exhibit a charge/discharge voltage of 2.01/1.04 V and a voltage gap of 0.97 V. Moreover, the voltage gap keeps constant when the battery is bended at different angles. After 40 cycles, the voltage gap exhibited a slight increase to 1.06 V, and the charge/discharge voltage became 2.07/1.01 V (Fig. S17). The results reveal that the as-obtained o-CC-H_2 is a promising flexible electrocatalyst for the applications in wearable and portable devices. The flexibility is inherited from the carbon cloth, and the activity is contributed from the defective, oxygen-doped porous surface. This free-standing material are also applicable as a substrate to load other materials towards vast applications in flexible devices.

The Zn–air battery performances of o-CC-H_2 and other recently reported metal-free bifunctional electrocatalysts [28,34,56–59] are listed in Table S2. The o-CC-H_2 electrocatalyst shows comparable performance to the reported carbon materials with N, P or S heteroatom doped. It's promising that better Zn–air battery performance can be realized on the defect-rich porous carbon fiber material if more kinds of heteroatoms were introduced. For the future investigations on Zn–air batteries, Zn materials with high surface area, such as Zn powders and electrodeposited Zn films, are expected to be utilized as the Zn electrode to enhance the performance [60–63]. Moreover, as the alkaline electrolyte can react with the CO_2 in the air, near-neutral electrolyte is also worth studying for longer battery life [64–66].

Free-standing, flexible electrocatalysts for oxygen electrolysis have been researched by some works in recent years [34,35,51,55,58,59,67–71], and some of them also focus on the surface modification of carbon fibers [41,45,72]. However, to our knowledge, it's for the first time that a porous graphene skin with both porous exfoliated graphene sheets and large surface graphitic pores is facilely generated from the carbon fiber. Specifically, the pores with a size less than 100 nm are regularly, densely distributed on the surface of carbon fibers with a depth about 300 nm, forming a defect-rich and coaxial cable-like structure. This modified carbon cloth was employed in a flexible Zn–air battery. This unique structure enlarges the surface area of carbon fibers, and allows more heteroatom doping and more defects to enhance the electrocatalytic activity. This o-CC-H_2 material reported herein also features the following novel characteristics: (1) A porous and defect-rich graphene skin is formed on the surface on carbon cloth for oxygen electrocatalysis, and the active sites are derived from the carbon cloth substrate directly. (2) This material with *in situ* generated surface pores shows the potential to be a substrate for the synthesis of new types of materials. Functional nanoparticles can be deposited on the surface and confined within the surface pores. (3) The active porous graphene skin and the carbon fiber substrate have strong interaction. (4) The synthesis method provides a simple approach towards the nanostructured surface of carbon fibers. Carbon cloth used to be applied as inactive substrate in many energy devices. This work can provide some new insights into this material, that through rational modification, carbon cloth can be active for certain reactions. Based on the H_2-

etching method proposed in this contribution, we can create a variety of nanostructures on the surface of carbon fibers for energy applications.

3. Conclusions

A nanostructured defect-rich, surface porous, coaxial cable-like electrocatalyst based on carbon fibers is proposed for bifunctional electrocatalysis of OER and ORR in this work. A facile H_2-etching approach is applied to *in situ* obtain the porous graphene skin on the surface of carbon fibers. Porous graphene sheets are exfoliated directly on the surface with some macropores regularly and densely distributed, which are accompanied with abundant oxygen-containing groups and defects as active sites. With these advantages, the o-CC-H_2 material exhibits superior activity on oxygen electrocatalysis. The E_{10} for OER is 1.618 V and the ORR peak potential is 0.565 V, significantly improved compare with the pristine CC. When employed as the air electrode in flexible solid-state Zn–air battery, o-CC-H_2 delivers an open-circuit voltage of 1.258 V, and a stable charge/discharge voltage gap of 0.97 V at the current density of 1.0 mA cm^{-2}. The design principle and synthetic strategy presented here are expected to open new doors for the application of carbon fiber-based materials in various fields, such as electrocatalysis, supercapacitors and batteries.

Acknowledgment

This work was supported by National Key Research and Development Program (2016YFA0202500 and 2016YFA0200102), National Natural Scientific Foundation of China (21676160 and 21706146), Fok Ying Tung Education Foundation (160166), and China Postdoctoral Science Foundation (2016M600097). We thank helpful discussion with Zi-Jing Xia and Ling Zhong.

Appendix A. Supplementary material

Supplementary data associated with this article can be found in the online version at doi:10.1016/j.ensm.2018.03.022.

References

[1] J.S. Lee, S.T. Kim, R. Cao, N.S. Choi, M. Liu, K.T. Lee, J. Cho, Adv. Energy Mater. 1 (2011) 34–50.
[2] Y.G. Li, H.J. Dai, Chem. Soc. Rev. 43 (2014) 5257–5275.
[3] J. Fu, Z.P. Cano, M.G. Park, A.P. Yu, M. Fowler, Z.W. Chen, Adv. Mater. 29 (2017) 1604685.
[4] S. Chen, J.J. Duan, Y. Zheng, X.M. Chen, X.W. Du, M. Jaroniec, S.Z. Qiao, Energy Storage Mater. 1 (2015) 17–24.
[5] H.H. Wu, X.L. Jiang, Y.F. Ye, C.C. Yan, S.H. Xie, S. Miao, G.X. Wang, X.H. Bao, J. Energy Chem. 26 (2017) 1181–1186.
[6] C. Tang, B. Wang, H.F. Wang, Q. Zhang, Adv. Mater. 29 (2017) 1703185.
[7] A. Sumboja, M. Lubke, Y. Wang, T. An, Y. Zong, Z.L. Liu, Adv. Energy Mater. 7 (2017) 1700927.
[8] C.Y. Su, H. Cheng, W. Li, Z.Q. Liu, N. Li, Z.F. Hou, F.Q. Bai, H.X. Zhang, T.Y. Ma, Adv. Energy Mater. 7 (2017) 1602420.
[9] X. Chen, B. Liu, C. Zhong, Z. Liu, J. Liu, L. Ma, Y.D. Deng, X.P. Han, T.P. Wu, W.B. Hu, J. Lu, Adv. Energy Mater. 7 (2017) 1700779.
[10] L. An, Y.X. Li, M.C. Luo, J. Yin, Y.Q. Zhao, C.L. Xu, F.Y. Cheng, Y. Yang, P.X. Xi, S.J. Guo, Adv. Funct. Mater. 27 (2017) 1703779.
[11] C. Guan, A. Sumboja, H.J. Wu, W.N. Ren, X.M. Liu, H. Zhang, Z.L. Liu, C.W. Cheng, S.J. Pennycook, J. Wang, Adv. Mater. 29 (2017) 1704117.
[12] H. Cheng, J.M. Chen, Q.J. Li, C.Y. Su, A.N. Chen, J.X. Zhang, Z.Q. Liu, Y.X. Tong, Chem. Commun. 53 (2017) 11596–11599.
[13] S.X. Qu, Z.S. Song, J. Liu, Y.B. Li, Y. Kou, C. Ma, X.P. Han, Y.D. Deng, N.Q. Zhao, W.B. Hu, C. Zhong, Nano Energy 39 (2017) 101–110.
[14] S.S. Shinde, J.Y. Yu, J.W. Song, Y.H. Nam, D.H. Kim, J.H. Lee, Nanoscale Horiz. 2 (2017) 333–341.
[15] C. Lin, S.S. Shinde, Y. Wang, Y. Sun, S. Chen, H.J. Zhang, X.P. Li, J.H. Lee, Sustain. Energy Fuels 1 (2017) 1909–1914.
[16] A.R. Ugalde, H.E. Naguib, Energy Storage Mater. 8 (2017) 1–9.
[17] Z.Q. Wang, X.Y. Meng, Z.Q. Wu, S. Mitra, J. Energy Chem. 26 (2017) 129–138.
[18] J. Pan, Y.Y. Xu, H. Yang, Z. Dong, H. Liu, B.Y. Xia, Adv. Sci. 5 (2018) 1700691.
[19] D.J. Yang, L.J. Zhang, X.C. Yan, X.D. Yao, Small Methods 1 (2017) 1700209.
[20] F.Y. Cheng, J. Chen, Chem. Soc. Rev. 41 (2012) 2172–2192.
[21] Y. Jiao, Y. Zheng, M.T. Jaroniec, S.Z. Qiao, Chem. Soc. Rev. 44 (2015) 2060–2086.
[22] N.-T. Suen, S.-F. Hung, Q. Quan, N. Zhang, Y.-J. Xu, H.M. Chen, Chem. Soc. Rev. 46 (2017) 337–365.
[23] F.Y. Cheng, J.A. Shen, B. Peng, Y.D. Pan, Z.L. Tao, J. Chen, Nat. Chem. 3 (2011) 79–84.
[24] Y. Gorlin, T.F. Jaramillo, J. Am. Chem. Soc. 132 (2010) 13612–13614.
[25] H. Osgood, S.V. Devaguptapu, H. Xu, J. Cho, G. Wu, Nano Today 11 (2016) 601–625.
[26] C. Tang, H.F. Wang, X. Chen, B.Q. Li, T.Z. Hou, B.S. Zhang, Q. Zhang, M.M. Titirici, F. Wei, Adv. Mater. 28 (2016) 6845–6851.
[27] H.B. Yang, J.W. Miao, S.F. Hung, J.Z. Chen, H.B. Tao, X.Z. Wang, L.P. Zhang, R. Chen, J.J. Gao, H.M. Chen, L.M. Dai, B. Liu, Sci. Adv. 2 (2016) e1501122.
[28] J.T. Zhang, Z.H. Zhao, Z.H. Xia, L.M. Dai, Nat. Nanotechnol. 10 (2015) 444–452.
[29] X.Q. Zhang, X.B. Cheng, Q. Zhang, J. Energy Chem. 25 (2016) 967–984.
[30] Y.G. Li, M. Gong, Y.Y. Liang, J. Feng, J.E. Kim, H.L. Wang, G.S. Hong, B. Zhang, H.J. Dai, Nat. Commun. 4 (2013) 1805.
[31] H.F. Wang, C. Tang, B. Wang, B.Q. Li, Q. Zhang, Adv. Mater. (2017) 1702327.
[32] Q. Wang, L. Shang, R. Shi, X. Zhang, Y. Zhao, G.I.N. Waterhouse, L.Z. Wu, C.H. Tung, T. Zhang, Adv. Energy Mater. 7 (2017) 1700467.
[33] P.Z. Chen, K. Xu, Z.W. Fang, Y. Tong, J.C. Wu, X.L. Lu, X. Peng, H. Ding, C.Z. Wu, Y. Xie, Angew. Chem. Int. Ed. 54 (2015) 14710–14714.
[34] T.Y. Ma, J.R. Ran, S. Dai, M. Jaroniec, S.Z. Qiao, Angew. Chem. Int. Ed. 54 (2015) 4646–4650.
[35] R. Chen, H.Y. Wang, J.W. Miao, H.B. Yang, B. Liu, Nano Energy 11 (2015) 333–340.
[36] J.W. Miao, F.X. Xiao, H.B. Yang, S.Y. Khoo, J. Chen, Z. Fan, Y.Y. Hsu, H.M. Chen, H. Zhang, B. Liu, Sci. Adv. 1 (2015) e1500259.
[37] M.J. Behr, B.G. Landes, B.E. Barton, M.T. Bernius, G.F. Billovits, E.J. Hukkanen, J.T. Patton, W.J. Wang, C. Wood, D.T. Keane, J.E. Rix, S.J. Weigand, Carbon 107 (2016) 525–535.
[38] D.F. Yan, Y.X. Li, J. Huo, R. Chen, L.M. Dai, S.Y. Wang, Adv. Mater. 29 (2017) 1606459.
[39] C. Tang, M.M. Titirici, Q. Zhang, J. Energy Chem. 26 (2017) 1077–1093.
[40] C. Tang, H.F. Wang, Q. Zhang, Acc. Chem. Res. 51 (2018). http://dx.doi.org/10.1021/acs.accounts.7b00616.
[41] Z.J. Liu, Z.H. Zhao, Y.Y. Wang, S. Dou, D.F. Yan, D.D. Liu, Z.H. Xia, S.Y. Wang, Adv. Mater. 29 (2017) 1606207.
[42] J.F. Sun, F. Zhao, Y. Yao, X. Liu, Z. Jin, Y.D. Huang, Mater. Lett. 196 (2017) 46–49.
[43] L.F. Hao, P. Peng, F. Yang, B.Y. Zhang, J. Zhang, X.L. Lu, W.C. Jiao, W.B. Liu, R.G. Wang, X.D. He, Carbon 114 (2017) 317–323.
[44] G.L. Tian, Q. Zhang, B.S. Zhang, Y.G. Jin, J.Q. Huang, D.S. Su, F. Wei, Adv. Funct. Mater. 24 (2014) 5956–5961.
[45] N.Y. Cheng, Q. Liu, J.Q. Tian, Y.R. Xue, A.M. Asiri, H.F. Jiang, Y.Q. He, X.P. Sun, Chem. Commun. 51 (2015) 1616–1619.
[46] Y. Zhao, R. Nakamura, K. Kamiya, S. Nakanishi, K. Hashimoto, Nat. Commun. 4 (2013) 2390.
[47] Y. Jia, L.Z. Zhang, A.J. Du, G.P. Gao, J. Chen, X.C. Yan, C.L. Brown, X.D. Yao, Adv. Mater. 28 (2016) 9532–9538.
[48] C. Tang, Q. Zhang, Adv. Mater. 29 (2017) 1604103.
[49] C.M. Chen, Q. Zhang, M.G. Yang, C.H. Huang, Y.G. Yang, M.Z. Wang, Carbon 50 (2012) 3572–3584.
[50] Z.W. Seh, J. Kibsgaard, C.F. Dickens, I.B. Chorkendorff, J.K. Norskov, T.F. Jaramillo, Science 355 (2017) 146.
[51] S. Chen, J.J. Duan, M. Jaroniec, S.Z. Qiao, Adv. Mater. 26 (2014) 2925–2930.
[52] X.Y. Lu, W.L. Yim, B.H.R. Suryanto, C. Zhao, J. Am. Chem. Soc. 137 (2015) 2901–2907.
[53] J. Zhang, H. Zhou, J.W. Zhu, P. Hu, C. Hang, J.L. Yang, T. Peng, S.C. Mu, Y.H. Huang, ACS Appl. Mater. Interfaces 9 (2017) 24545–24554.
[54] G.L. Chai, K.P. Qiu, M. Qiao, M.M. Titirici, C.X. Shang, Z.X. Guo, Energy Environ. Sci. 10 (2017) 1186–1195.
[55] J.C. Li, P.X. Hou, S.Y. Zhao, C. Liu, D.M. Tang, M. Cheng, F. Zhang, H.M. Cheng, Energy Environ. Sci. 9 (2016) 3079–3084.
[56] Z.X. Pei, H.F. Li, Y. Huang, Q. Xue, Y. Huang, M.S. Zhu, Z.F. Wang, C.Y. Zhi, Energy Environ. Sci. 10 (2017) 742–749.
[57] Z.J. Wang, Y.Z. Lu, Y. Yan, T.Y.P. Larissa, X. Zhang, D. Wuu, H. Zhang, Y.H. Yang, X. Wang, Nano Energy 30 (2016) 368–378.
[58] S.S. Shinde, C.H. Lee, A. Sami, D.H. Kim, S.U. Lee, J.H. Lee, ACS Nano 11 (2017) 347–357.
[59] Q. Liu, Y.B. Wang, L.M. Dai, J.N. Yao, Adv. Mater. 28 (2016) 3000–3006.
[60] H. Ma, C.S. Li, Y. Su, J. Chen, J. Mater. Chem. 17 (2007) 684–691.
[61] C.C. Yang, S.J. Lin, J. Power Sources 112 (2002) 174–183.
[62] X. Chen, B. Liu, C. Zhong, Z. Liu, J. Liu, L. Ma, Y.D. Deng, X.P. Han, T.P. Wu, W.B. Hu, J. Lu, Adv. Energy Mater. 7 (2017) 1700779.
[63] L. Ma, S. Chen, Z. Pei, Y. Huang, G. Liang, F. Mo, Q. Yang, J. Su, Y. Gao, J.A. Zapien, C. Zhi, ACS Nano 12 (2018) 1949–1958.
[64] J. Stamm, A. Varzi, A. Latz, B. Horstmann, J. Power Sources 360 (2017) 136–149.
[65] F.W.T. Goh, Z.L. Liu, T.S.A. Hor, J. Zhang, X.M. Ge, Y. Zong, A.S. Yu, W. Khoo, J. Electrochem. Soc. 161 (2014) A2080–A2086.
[66] J.F. Drillet, F. Holzer, T. Kallis, S. Muller, V.M. Schmidt, Phys. Chem. Chem. Phys. 3 (2001) 368–371.
[67] H. Wang, S.X. Min, C. Ma, Z.X. Liu, W.Y. Zhang, Q. Wang, D.B. Li, Y.Y. Li, S. Turner, Y. Han, H.B. Zhu, E. Abou-Hamad, M.N. Hedhili, J. Pan, W.L. Yu, K.W. Huang, L.J. Li, J.Y. Yuan, M. Antonietti, T. Wu, Nat. Commun. 8 (2017) 13592.
[68] J. Fu, F.M. Hassan, J.D. Li, D.U. Lee, A.R. Ghannoum, G. Lui, M.A. Hoque, Z.W. Chen, Adv. Mater. 28 (2016) 6421–6428.
[69] Z.H. Li, M.F. Shao, Q.H. Yang, Y. Tang, M. Wei, D.G. Evans, X. Duan, Nano Energy 37 (2017) 98–107.
[70] S. Zeng, H.Y. Chen, H. Wang, X. Tong, M.H. Chen, J.T. Di, Q.W. Li, Small 13 (2017) 1700518.
[71] X.Y. Cai, B.Y. Xia, J. Franklin, B.S. Li, X. Wang, Z. Wang, L.W. Chen, J.Y. Lin, L.F. Lai, Z.X. Shen, J. Mater. Chem. A 5 (2017) 2488–2495.
[72] M.S. Balogun, W.T. Qiu, H. Yang, W.J. Fan, Y.C. Huang, P.P. Fang, G.R. Li, H.B. Ji, Y.X. Tong, Energy Environ. Sci. 9 (2016) 3411–3416.